Hyperfine spectra of the radioactive isotopes ^{81}Kr and ^{85}Kr

B. D. Cannon
Pacific Northwest Laboratory, MS P8-08, P.O. Box 999, Richland, Washington 99352
(Received 6 July 1992)

Isotope shifts and hyperfine constants are reported for the radioactive isotopes ^{81}Kr and ^{85}Kr and the stable isotope ^{83}Kr. The previously unreported nuclear moments of ^{81}Kr were determined to be $\mu_I = -0.909(4)$ nuclear magneton and $Q = +0.630(13)$ b from the hyperfine constants. This work increases the number of transitions for which ^{85}Kr hyperfine constants and isotope shifts have been measured from 1 to 4. The hyperfine anomaly for krypton reported in the previous measurement of ^{85}Kr hyperfine constants [H. Gerhardt *et al.*, Hyperfine Interact. **9**, 175 (1981)] is not supported by this work. The isotope shifts and hyperfine constants of ^{83}Kr measured in this work are in excellent agreement with previous work. Saturation spectroscopy was used to study transitions from krypton's metastable $1s_5$ state to the $2p_9$, $2p_7$, and $2p_6$ states. In saturation spectra, different line shapes were observed for the even- and odd-mass krypton isotopes. This even- versus odd-line-mass shape difference can be explained using the large cross section that has been reported for collisional transfer of the $1s_5$ state excitation between krypton atoms. Two-color two-photon laser-induced fluorescence was used to measure the hyperfine spectra of the $1s_5$-$4d'_4$ transition using the $2p_9$ state as the intermediate state. This technique proved to be more sensitive than saturation spectroscopy.

PACS number(s): 32.30.Jc, 27.50.+e, 32.70.Jz

I. INTRODUCTION

Hyperfine spectroscopy is a classic technique for determining nuclear spin and nuclear moments [1] and it provides information on isotopic changes in the nuclear charge distribution [2,3], on the electron wave function at the nucleus, and on electron correlation and configuration mixing [4,5]. Hyperfine interactions are separated into two groups: (1) isotope shifts, which are present for all isotopes and electronic states, and (2) hyperfine structure, which occurs only when both the nuclear and electronic angular momenta are nonzero. Because these hyperfine interactions are usually much smaller than the separations between electronic states, first-order perturbation theory is a good approximation [6]. The first-order treatment gives scaling relationships that can be used to check the consistency of hyperfine measurements and to accurately predict hyperfine splittings. These splittings are also used to evaluate laser-based ultrasensitive isotopic analysis techniques.

The hyperfine spectroscopy of the stable krypton isotopes has been extensively studied for both the stable even-mass isotopes [7–14] and the stable odd-mass isotope, ^{83}Kr [7,13–20]. Isotope shifts for two radioactive even-mass krypton isotopes, ^{88}Kr and ^{90}Kr, were reported recently [21]. There has been little study of the hyperfine spectra of the two long-lived radioactive krypton isotopes, ^{81}Kr and ^{85}Kr whose half-lives are, respectively, 2.1×10^5 and 10.76 yr. For ^{81}Kr, no nuclear moments, hyperfine constants, or isotope shifts have been reported. For ^{85}Kr, there are two hyperfine studies in the literature: an emission study [22] and a saturated absorption study [23,24]. The emission study determined the nuclear spin and nuclear moments of ^{85}Kr though the precision on the quadrupole moment was low. From the single ^{85}Kr transition measured in the saturated absorption study, the authors reported a hyperfine anomaly for the magnetic-dipole hyperfine constant of 0.8(3)% [23]. A hyperfine anomaly is a deviation from the first-order prediction of simple proportional scaling of hyperfine constants between isotopes. This same study found no breakdown for xenon to the 0.05% level. Both elements have similar electronic and nuclear structure and given its larger nucleus, xenon would be expected to have the larger hyperfine anomaly. Thus the reported anomaly for krypton is surprising.

There are applications for ultrasensitive measurement of ^{81}Kr and ^{85}Kr in the fields of fundamental physics, climatology, hydrology, and atmospheric transport. A proposed solar-neutrino experiment [25] requires measuring the production of few ^{81}Kr atoms from tons of ^{81}Br. With its 2.1×10^5-yr half-life, ^{81}Kr has applications for dating on the time scale of 10^5–10^6 yr [26,27]. The dating role arises because ^{81}Kr is produced by cosmic rays in the atmosphere and not below the earth's surface. Dating ice from deep within glaciers would help in understanding climatic change. Ground water dating would help characterize both potential radioactive waste burial sites and aquifers with long recharging times [28,29]. The presence of ^{85}Kr would indicate sample contamination by modern air or ground water [26,28]. Other applications for ^{85}Kr measurement involve dating ground water less than 30 years old [26] and monitoring atmospheric transport of radioactive contamination following nuclear accidents [26] such as the one that occurred at Chernobyl. Prompted by these applications, several laser-based techniques have been proposed [30–32] and one has been demonstrated [33] for these measurements. Knowledge of ^{81}Kr and ^{85}Kr hyperfine spectra is needed to evaluate and demonstrate the feasibility of some of

these approaches.

Hyperfine spectra of ^{81}Kr and ^{85}Kr were measured using both saturation spectroscopy and two-color two-photon spectroscopy. After my measurements were completed I learned of recent unpublished measurements of ^{81}Kr and ^{85}Kr hyperfine spectra for one transition [46]. The results of my work do not support the reported [23] hyperfine anomaly in krypton. A surprising finding in my saturation spectra is the difference in the Doppler background between the even and odd isotopes. The transitions of the even isotopes have 10 to 100 times larger Doppler backgrounds than the odd-isotope transitions. This difference is consistent with a model [35] for the saturated absorption line shapes in krypton. The large cross section in this model for collision-induced electronic energy transfer between krypton atoms is key to modeling my observed differences in the line shapes of even versus odd isotopes.

II. EXPERIMENT

These measurements required a high-resolution Doppler-free technique because of the small isotope shifts and hyperfine splittings. High sensitivity and selectivity were needed for the small dilute samples that were used. The Doppler-free technique of saturated intermodulated fluorescence met these needs. Due to a fortunate combination of energy levels, two-color two-photon laser-induced fluorescence of the $1s_5$-$4d'_4$ transition was more sensitive and selective than the saturation technique. Table I gives the excitation transitions used in this work in both Pashen and Racah notation [36]. The transitions used for detection and the excitation and detection wavelengths are also shown in Table I.

Because the samples were radioactive, a static gas cell was used to minimize sample size, release of radioactive krypton, and the amount of potentially contaminated equipment. Efficient production of krypton metastables in a static cell requires great care in cell preparation and sample purification, which are described in some detail.

Figure 1 is a schematic diagram of the experimental apparatus. A 40-MHz radio frequency (rf) source sustained a weak discharge in a 2-cm path-length cell (Hel-

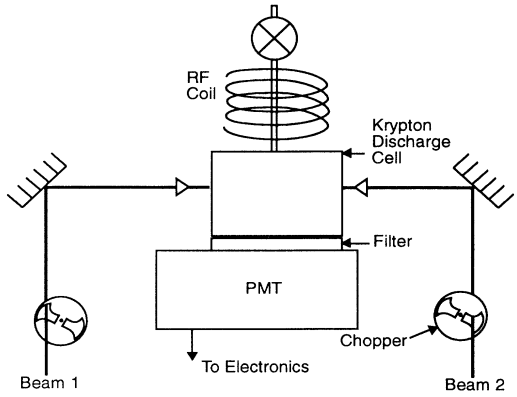

FIG. 1. Experimental schematic of the apparatus for both the saturation and the two-color two-photon laser-induced-fluorescence experiments. For saturation spectra, both laser beams come from a cw single-frequency dye laser. For the two-photon spectra, beam 1 at 811.5 nm is from a frequency-narrowed diode laser and beam 2 is from the dye laser. Only beam 2 is chopped for the two-photon spectra. PMT denotes a photomultiplier tube.

ma model 225PY-20) containing less than 100 mtorr of krypton. The fluorescence induced by a pair of counter-propagating laser beams (5 mm diameter) was detected by a photomultiplier tube (PMT) through an interference filter. A lock-in amplifier (Stanford Research Systems Model SR510) detected the signal at the sum of the chopping frequencies of the two beams (typically 480 Hz plus 640 Hz) for saturation spectra. For the two-color two-photon spectra of the $1s_5$-$4d'_4$ transition, only the second laser beam at 810.6 nm was chopped as this gave the best signal-to-noise ratio. Figure 2 shows the energy levels involved in the excitation and detection for the two-photon spectra.

In a continuous discharge, used for the ^{85}Kr $1s_5$-$2p_9$ transition, typically 1 W of rf power was incident on a helical resonator [37,38] surrounding the stem of the cell. Most of the incident power was reflected. For all other transitions, a pulsed discharge was used. For the pulsed discharge, a pulsed rf source replaced the continuous rf

TABLE I. Paschen and Racah notation for the transitions studied in this work, their vacuum wavelengths, the transition used for detection, and its vacuum wavelength.

Paschen	Racah	Excitation wavelength (nm)	Detection wavelength (nm)	Detection transition
$1s_5$-$2p_6$	$5s[\frac{3}{2}]_2$-$5p[\frac{3}{2}]_2$	760.4	819.2	$1s_4$-$2p_6$
$1s_5$-$2p_7$	$5s[\frac{3}{2}]_2$-$5p[\frac{3}{2}]_1$	769.7	830.0	$1s_4$-$2p_7$
$1s_5$-$2p_9$	$5s[\frac{3}{2}]_2$-$5p[\frac{5}{2}]_3$	811.5	811.5	$1s_5$-$2p_9$
$1s_5$-$4d'_4$	$5s[\frac{3}{2}]_2$-$5d[\frac{7}{2}]_4$	811.5+810.6	432.0	$1s_5$-$3p_9$

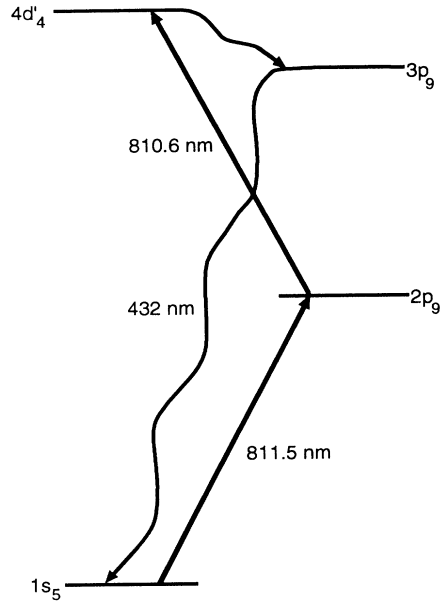

FIG. 2. Energy levels, excitation path ($1s_5$-$2p_9$-$4d'_4$), and detection path for the two-color two-photon spectra. The two excitation wavelengths are 811.5 and 810.6 nm and the intermediate state is the $2p_9$ state. The $4d'_4$ level decays by spontaneous emission and collisions to the $3p_9$ state, which decays by emission at 432 nm to the $1s_5$ state.

source. This source sent 10-μs, 10-W pulses at a 10-kHz repetition rate to the helical resonator that reflected most of the power. There was no significant decay of the population of krypton in the $1s_5$ state, Kr($1s_5$), between pulses. However, the background light from the discharge disappeared a few microseconds after the end of the rf pulse. The PMT signal, terminated into 10 kΩ, was amplified by a low-noise preamplifier with a gain of 10. A boxcar integrator (Stanford Research Systems SR250, 15-μs gate width) sampled the amplified signal 50 μs after each rf pulse and provided the sampled signal to a lock-in amplifier referenced to the appropriate frequency as described above. This procedure reduced the background noise level by a factor of about 3 from that found with the continuous discharge. Shot noise due to background light from the discharge is the dominant noise source in experiments with a continuous discharge. With the pulsed configuration, electronic noise from the preamplifier and boxcar integrator each contributed about half the noise.

A different cell was used for each sample including a reference cell of natural krypton. Each cell contained a nonevaporable getter pellet (Saes Getters Model ST 707) and was baked to 400 °C while being pumped to less than 1×10^{-6} Torr. This baking removed volatile impurities and activated the getter pellet. Stable krypton discharges and high metastable concentrations require high purity in the discharge cells.

Natural krypton was purified by several freeze-pump-thaw cycles using liquid nitrogen. The reference cell was filled with krypton vapor from a reservoir immersed in liquid nitrogen. The radioactive krypton samples were transferred to stainless steel reservoirs containing 1 g of activated coconut charcoal. Baking at 500 °C for several hours under vacuum cleaned the activated charcoal before its use in the reservoir. Quartz wool kept the charcoal in place. After assembling the reservoirs, the activated charcoal was baked at 400 °C and pumped to less than 10^{-6} Torr for several hours. With the charcoal at liquid-nitrogen temperature, the krypton vapor pressure was about 10^{-5} Torr. Initially adding krypton to the reservoirs displaced adsorbed molecules from the activated charcoal. To remove these impurities, the gas from the reservoir was exposed to getter pellets heated to 400 °C. Repeatedly condensing and evaporating the krypton sample ensured the gas was well mixed. Heating the sealed cell containing a getter pellet to 400 °C accomplished the final sample cleaning. This left a black deposit inside the cell that increased the scattered light level. However, this cleaning was essential to obtaining a stable discharge and a sufficient concentration of Kr($1s_5$).

A new discharge cell filled with 50 mTorr of krypton will sustain a discharge for only a few minutes. A plasma sheath forms at the cell walls creating a dc potential [39] that implants krypton ions into the glass cell walls [40]. This ion implantation pumps krypton until the discharge is extinguished. A weak rf discharge in a 30-cm-long by 12-mm-diameter Pyrex tube will pump a 0.2-l vacuum manifold from 20 mTorr of krypton to below 1 mTorr in a couple of hours. Heating a discharge cell to 400 °C releases krypton from the glass, in agreement with previous results [40]. To obtain a low-pressure discharge that is stable for several hours requires several refills with 50 mTorr of krypton. A higher initial krypton pressure (e.g., 200 mTorr) also will give a stable discharge but the higher pressure slows the rate of implantation and reduces the Doppler-free signals.

The ^{81}Kr sample (donated by Frank Shima of the National Institute of Standards and Technology) contained about 0.3% ^{81}Kr, 3% ^{83}Kr, 50% ^{80}Kr, 20% ^{78}Kr, 25% ^{82}Kr, and 0.3% ^{84}Kr. It was made by irradiating a krypton sample enriched to 50% ^{80}Kr in the National Bureau of Standards' research reactor in 1974. The ^{85}Kr sample (Oak Ridge Isotope Sales, Oak Ridge National Laboratory) contained 2.5% ^{85}Kr and 97.5% ^{86}Kr with any other isotopes less than 0.1%. Low-pressure (estimated to be 5–10 mTorr) saturation spectra of the $1s_5$-$2p_9$ transition were used to identify the even isotopes in these samples by comparison with natural krypton samples.

A standing-wave cw single-frequency dye laser (Coherent 599-21) was used in these experiments. For the two-color two-photon experiments, a frequency-narrowed diode laser [41] provided the first color. A fringe-offset lock technique, which is described in detail elsewhere [42], controlled the laser frequency (or frequencies). This control system reduces drift and gives a calibrated linear frequency scan. The accuracy of this system was demonstrated in earlier work [14] where agreement with microwave measurements [17] of the A hyperfine constant of ^{83}Kr($1s_5$) was within 0.02%. The wavelengths of the single-frequency lasers were measured with a homemade

wavemeter [42] with a resolution of 10^7 that was referenced to a single-frequency helium-neon laser. The krypton excitation wavelengths were taken from the tabulations of Kaufman and Humphreys [43] and Moore [36].

Neither the single-frequency dye laser nor the frequency-narrowed diode laser is perfectly of single-frequency type. The dye laser has sidebands at ± 848 MHz from the center frequency, which corresponds to three times the longitudinal mode spacing of the dye laser. The frequency-narrowed diode laser has sidebands at ± 765 MHz from the center frequency. These sidebands are less than 0.1% the intensity of the central frequency. However, they still produced spurious peaks in the two-color two-photon spectra that complicated identification of the ^{81}Kr lines. The sidebands did not cause problems in the saturation spectra because the strong even-isotope peak was so broad.

III. RESULTS

The energies of hyperfine levels ν_F relative to a reference energy level are described by

$$\nu_F = \nu_J + A(C/2) + B\frac{\frac{3}{4}C(C+1) - I(I+1)J(J+1)}{2I(2I-1)J(2J-1)}, \quad (1)$$

where F, J, and I are, respectively, the total, the electronic, and the nuclear spin angular momentum quantum numbers and $C = F(F+1) - I(I+1) - J(J+1)$. A and B, respectively, are the magnetic-dipole and electric-quadrupole hyperfine constants, and ν_J is the center-of-mass shift relative to the reference energy level. By using Eq. (1) for the upper and lower states of a transition, the peak positions in the hyperfine spectrum of an isotope can be calculated from five constants: the A's and B's for the two states and the transition isotope shift from a reference isotope. I chose ^{83}Kr as the reference in this work. The transition isotope shift is the difference between the isotope shifts for the upper and lower states of the transition. A weighted linear least-squares fit to the observed peak positions determined these constants and typically used the positions of ten peaks.

To determine peak positions, the baseline was subtracted over a limited region using a polynomial approximation. A nonlinear least-squares program fit a Lorentzian line shape to the peaks in the baseline subtracted data. Peak positions from typically three or four spectra were averaged. The weighting for the least-squares fit was the one-standard-deviation error estimate of the average peak position. Highly blended lines were not used in the least-squares fit.

Figure 3 shows a saturation spectrum of the $1s_5$-$2p_6$ transition for the ^{85}Kr sample. The ^{85}Kr peak amplitudes are 10^{-3} to 10^{-4} smaller than the ^{86}Kr peak. The technique of pulsed rf excitation and gated detection was crucial to observing the weaker peaks in this spectrum. The most striking feature of the saturation spectrum in Fig. 3 is how different the ^{86}Kr and ^{85}Kr peak shapes are. This difference in peak shapes between the even and odd isotopes is a general feature of my saturation spectra, which

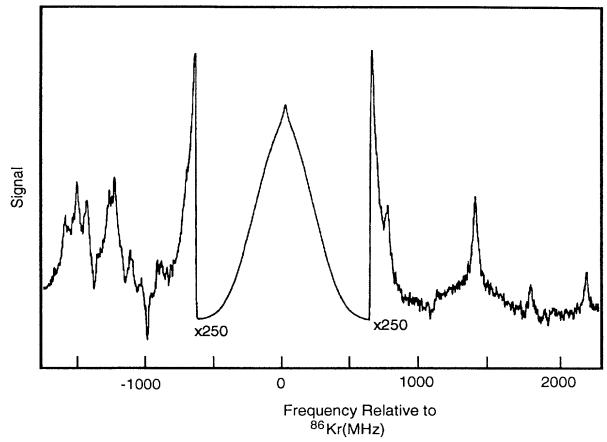

FIG. 3. Saturation spectrum of the $1s_5$-$2p_6$ transition with the ^{85}Kr sample which contains only ^{85}Kr and ^{86}Kr. The broad peak at zero is ^{86}Kr. The much larger Doppler background for ^{86}Kr than for ^{85}Kr is discussed in the text.

was observed for all transitions studied in natural krypton as well as the ^{81}Kr and ^{85}Kr samples. Rapid collisional transfer of $1s_5$ state excitation between isotopes can explain this difference as will be discussed below.

Figure 4 shows a two-color two-photon spectrum of the $1s_5$-$4d'_4$ transition for the ^{81}Kr sample. The first laser was $+900$ MHz from the maximum of the Doppler-broadened $1s_5$-$2p_9$ transition. This maximum closely coincides with the ^{80}Kr line center. The three large peaks on the left in Fig. 4 are due to ^{78}Kr, ^{80}Kr, and ^{82}Kr in order of increasing frequency. The broad peak approxi-

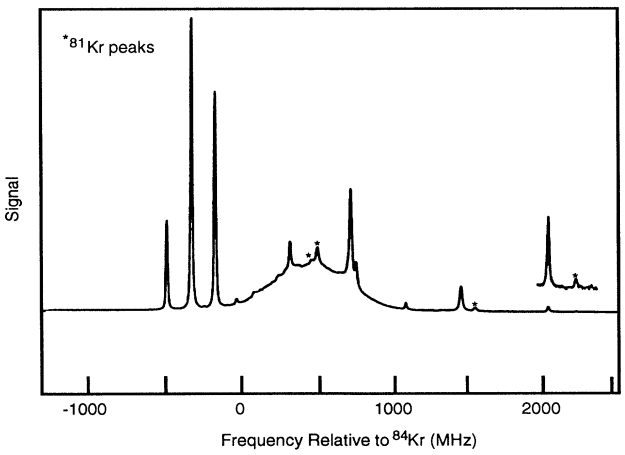

FIG. 4. Two-color two-photon spectrum of the $1s_5$-$4d'_4$ transition of the ^{81}Kr sample. The first laser at 811.5 nm is $+900$ MHz from the ^{80}Kr resonance in the $1s_5$-$2p_9$ transition and the second laser at 810.6 nm is scanned. The three large peaks at the left of the spectrum are from left to right ^{78}Kr, ^{80}Kr, and ^{82}Kr. The small peak at zero is ^{84}Kr and the remaining unmarked narrow peaks are ^{83}Kr. The broad peak is from the Doppler-broadened one-photon excitation of the $2p_9$-$4d'_4$ transition.

TABLE II. Isotope shifts of ^{81}Kr and ^{85}Kr relative to ^{83}Kr (in MHz). The numbers under the Δ heading are the differences between the measured shifts, $\delta\nu^{A,A+2}$, and half the isotope shift $\delta\nu^{A-1,A+3}$. As discussed in the text, Δ has no mass-shift component and should scale between pairs of transitions as the slope of the King plot. The numbers in parentheses are one-standard-deviation error estimates of the last digits shown.

	^{83}Kr-^{81}Kr		^{85}Kr-^{83}Kr	
Transition	Isotope shift	Δ	Isotope shift	Δ
$1s_5$-$2p_6$			60.6(30)[a]	−10.2(32)
	91.5(64)[b]	17.6(65)	60.8(64)[b]	−10.6(65)
$1s_5$-$2p_7$			59.7(20)[a]	−20.8(26)
$1s_5$-$2p_9$	85(5)[a,c]	16(5)	53.5(16)[a,d]	−11.6(19)
$1s_5$-$4d'_4$	184.0(27)[a]	24.0(48)		
$1s_5$-$2p_3$			75(1)[e]	−25(1)

[a]This work.
[b]Reference [46].
[c]Based on scaling hyperfine constants as described in the text.
[d]The value in [34] is wrong due to an arithmetic error.
[d]From Fig. 5 in [23] and parameter given in [10].

mately +900 MHz from the ^{80}Kr peak results from one-photon excitation of the $2p_9$-$4d'_4$ transition. The small peak at zero is due to ^{84}Kr; the remaining unmarked peaks are due to ^{83}Kr.

From left to right, the four ^{81}Kr peaks marked in Fig. 4 are the $(\frac{9}{2},\frac{9}{2})$, $(\frac{11}{2},\frac{15}{2})$, $(\frac{11}{2},\frac{13}{2})$, and $(\frac{11}{2},\frac{11}{2})$ transitions where (F,F') are, respectively, the lower and upper level hyperfine quantum numbers. Two additional ^{81}Kr hyperfine lines were observed in spectra with the first laser at the maximum of the Doppler-broadened transition. The ^{81}Kr hyperfine constants determined from this transition were scaled by the ^{83}Kr hyperfine constants to determine the ^{81}Kr hyperfine constants for the intermediate $2p_9$ state [see Eqs. (2) below]. From this prediction, the first laser is approximately +100 MHz from the $(\frac{11}{2},\frac{13}{2})$ line and −100 MHz from the $(\frac{9}{2},\frac{7}{2})$ line in the $1s_5$-$2p_9$ transition in ^{81}Kr. The four ^{81}Kr peaks identified in Fig. 4 are all resonantly enhanced via one of these two lines. The agreement between ^{81} Kr peaks observed and those predicted to be resonantly enhanced confirms that the assignment is correct. Resonance enhancement increases the intensity of these peaks relative to that of ^{80}Kr by about a factor of 200. This enhancement and the high signal levels of the two-color two-photon experiment allowed detection of peaks 5×10^4 times smaller than the ^{80}Kr peak.

Table II shows the isotope shifts of ^{81}Kr and ^{85}Kr with respect to ^{83}Kr measured in this work. Tables II–IV include the ^{85}Kr results of Gerhardt *et al.* [10,23] and measurements made at CERN-ISOLDE with a laser beam collinear with a mass separated fast beam of Kr($1s_5$) on ^{81}Kr and ^{85}Kr [46]. To my knowledge, these are the first published isotope shifts for ^{81}Kr and three of the transitions in ^{85}Kr. The only isotope shift in Table II that has been measured by more than one group is that of the $1s_5$-$2p_6$ transition of ^{85}Kr. Both these measurements agree to within their error estimates.

The isotope shift for the $1s_5$-$2p_9$ transition in ^{81}Kr was determined with a different method from that used for all the other isotope shifts. I found only one resolved ^{81}Kr line in the saturation spectra of the $1s_5$-$2p_9$ transition with the ^{81}Kr sample. Using the ^{81}Kr($1s_5$) hyperfine constants from the $1s_5$-$4d'_4$ spectra and ^{81}Kr($2p_9$) hyperfine constants calculated by proportional scaling reduced the problem to a one-parameter fit. This identified the single resolved ^{81}Kr peak as the $(\frac{11}{2},\frac{11}{2})$ line and determined the isotope shift. By comparing the predicted spectrum of the $1s_5$-$2p_9$ transition in ^{81}Kr with measured spectra, I found a second ^{81}Kr line blended with the $(\frac{11}{2},\frac{11}{2})$ line of ^{83}Kr. This unresolved ^{81}Kr peak was the $(\frac{11}{2},\frac{13}{2})$ line, the

TABLE III. Magnetic-dipole, A, and electric-quadrupole, B, hyperfine constants of ^{81}Kr in MHz. The numbers in parentheses are one-standard-deviation error estimates of the last digits shown.

State	A	B
$1s_5$	−294.02(27)[a]	−1117.2(48)[a]
	−293.41(48)[b]	−1127.8(43)[b]
$2p_6$	−130.52(36)[b]	−216.1(46)[b]
$4d'_4$	−88.19(19)[a]	−1147.2(55)[a]

[a]This work.
[b]Reference [46].

TABLE IV. Magnetic-dipole, A, and electric-quadrupole, B, hyperfine constants of ^{85}Kr in MHz. The numbers in parentheses are the one-standard-deviation error estimates of the last digits shown.

State	A	B
$1s_5$	−252.81(8)[a]	−775.8(12)[a]
	−252.7(3)[b]	−773.8(51)[b]
	−253.5(4)[c]	−775.6(27)[c]
$2p_9$	−107.56(10)[a]	−743.6(19)[a]
$2p_7$	−183.7(8)[a]	−116.7(43)[a]
$2p_6$	−112.46(14)[a]	−154.0(23)[a]
	−112.53(36)[b]	−147.9(65)[b]
$2p_3$	+232.9(3)[c]	+43.4(10)[c]

[a]This work.
[b]Reference [46].
[c]Reference [23].

TABLE V. Magnetic-dipole, A, and electric-quadrupole, B, hyperfine constants of ^{83}Kr in MHz. The numbers in parentheses are the one-standard-deviation error estimates of the last digits shown.

State	A	B
$1s_5$	−243.87(5)[a]	−453.1(7)[a]
	−243.93(4)[b]	−452.93(60)[b]
$2p_9$	−103.73(7)[a]	−438.8(12)[a]
	−104.02(6)[b]	−436.9(17)[b]
$2p_7$	−176.97(23)[a]	−66.5(10)[a]
	−176.80(18)[b]	−66.7(11)[b]
$2p_6$	−108.49(12)[a]	−85.7(16)[a]
	−108.61(11)[b]	−88.6(15)[b]
$4d'_4$	−73.66(2)[a]	−455.0(8)[a]
	−73.62(12)[b]	−459.1(40)[b]

[a]This work.
[b]Laser atomic-beam results from [14].

strongest ^{81}Kr hyperfine line in this transition. The relative amplitude and position of the $(\frac{11}{2},\frac{13}{2})$ line agreed well with the predicted spectrum. The identification of this second ^{81}Kr peak supports the determination of this isotope shift. The $(\frac{11}{2},\frac{13}{2})$ line of ^{81}Kr gave an isotope shift 4.5 MHz smaller than the $(\frac{11}{2},\frac{11}{2})$ ^{81}Kr line. Table II gives the average of these two determinations.

The hyperfine constants measured in this work for ^{81}Kr and ^{85}Kr are shown in Tables III and IV. For the two states for which there are other measurements, there is good agreement. In two cases the measurements differ by slightly more than the combined error estimates. The ^{85}Kr($1s_5$) hyperfine constants are the weighted average of the results of three transitions. The precision of the magnetic-dipole hyperfine constant is improved by a factor of 5 over the previous published value. The results of Neugart and co-workers are in good agreement with this work. Because the experiments in the fast beam and the cell are so different, the good agreement is evidence that any systematic errors in either experiment are less than the estimated errors.

Table V lists hyperfine constants measured in this work for ^{83}Kr. They are from spectra of ^{83}Kr present in both the ^{81}Kr sample and natural krypton used as a reference. The agreement of this work with our earlier atomic-beam measurements [14] is good with only the A values for the $2p_9$ state disagreeing by more than the error estimates. The precision for the $4d'_4$ hyperfine constants measured in this work is improved by a factor of 5 over our earlier atomic-beam results. This reflects the higher signal-to-noise ratio in the two-color two-photon experiment over the one-color two-photon atomic beam experiment. The agreement between the cell measurements and the atomic-beam measurements is further evidence for the absence of significant systematic errors.

The first-order treatment of the magnetic-dipole and electric-quadrupole interactions neglects the finite nuclear volume. Within this approximation, the scaling of the magnetic-dipole, A, and electric-quadrupole, B, hyperfine constants for electronic state α is given by [44]

$$\frac{^1A(\alpha)}{^2A(\alpha)}=\frac{\mu_I(1)}{\mu_I(2)}\frac{I(2)}{I(1)},$$
$$\frac{^1B(\alpha)}{^2B(\alpha)}=\frac{Q(1)}{Q(2)}, \tag{2}$$

for isotopes 1 and 2 where μ_I is the nuclear magnetic dipole moment, I is the nuclear spin, and Q is the electric-quadrupole moment. The right-hand sides of these two equations depend only on the nuclear moments and spins, not the electronic state.

The hyperfine constant ratios of Eqs. (2) are shown in Figs. 5 and 6 for the data in Tables III and IV. Figure 6 also shows the results of Rasmussen and Middelboe [22]. The electronic state independence of these ratios predicted by Eqs. (2) is observed and provides a consistency

TABLE VI. Nuclear moments of ^{81}Kr, ^{83}Kr, and ^{85}Kr. The magnetic-dipole moments are in nuclear magnetons and the electron-quadrupole moments are in barns.

Moment	^{81}Kr	^{83}Kr	^{85}Kr
μ_I	−0.909(4)[a]	−0.970 669(3)[b]	−1.0055(4)[a]
			−1.000(2)[c]
			−1.005(2)[d]
Q	+0.629(13)[a]	+0.253(5)[b]	+0.433(8)[a]
			+0.433(9)[c]
			+0.420(27)[d]

[a]This work.
[b]Reference [45].
[c]Reference [23].
[d]Reference [22].

check on both the spectral assignments and the nuclear spins. This is especially important for ^{81}Kr where only six ^{81}Kr hyperfine lines were found in the $1s_5$-$4d'_4$ transition. These hyperfine results confirm the spin of ^{81}Kr as $\frac{7}{2}$, which was determined from the radioactive decay branching ratios. The horizontal line in each figure shows the weighted average of all available data. These weighted averages of the ratios are $^{81}A/^{83}A = 1.2036(10)$, $^{85}A/^{83}A = 1.0359(3)$, $^{81}B/^{83}B = 2.487(7)$, and $^{85}B/^{83}B = 1.711(4)$.

Table VI shows the nuclear moments for ^{81}Kr and ^{85}Kr calculated using Eqs. (2), these averages of hyperfine constant ratios, and values for the moments of ^{83}Kr [45]. This calculation assumes that hyperfine anomalies and J mixing are negligible. This assumption is discussed below. The error estimates for the spectroscopic data dominate the error estimates for the nuclear magnetic-dipole moments of ^{81}Kr and ^{85}Kr. The uncertainty in the ^{83}Kr quadrupole moment determines the error estimates for the electric-quadrupole moments of ^{81}Kr and ^{85}Kr. Table VI also shows the ^{83}Kr nuclear moments and the previous results for ^{85}Kr [22,23].

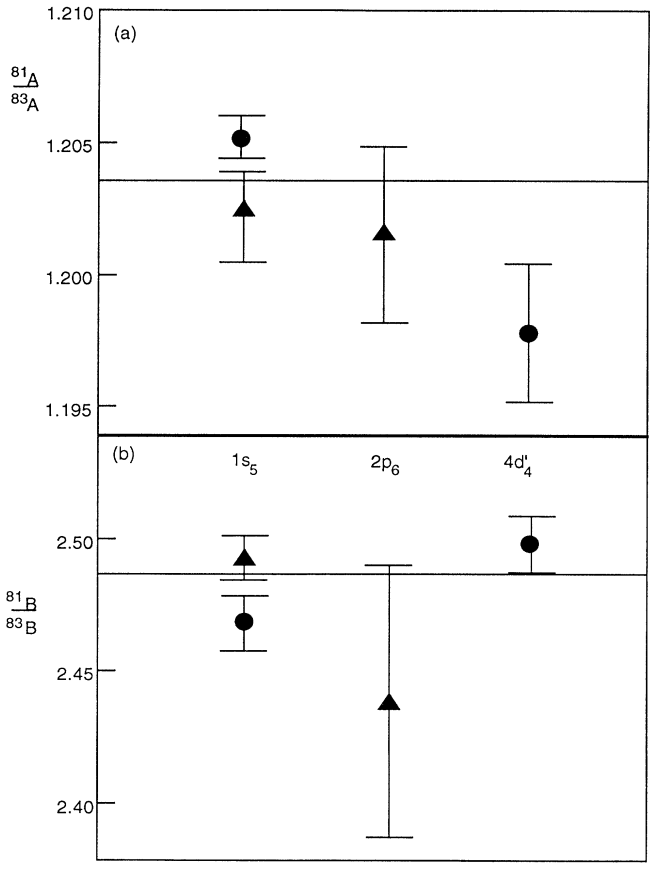

FIG. 5. Ratios of hyperfine constants of ^{81}Kr to ^{83}Kr; (a) $^{81}A/^{83}A$, (b) $^{81}B/^{83}B$. The solid circles are from this work and the solid triangles are from the work of Neugart [46]. The error bars represent one-standard-deviation error estimates. The horizontal lines are the weighted average of all the data.

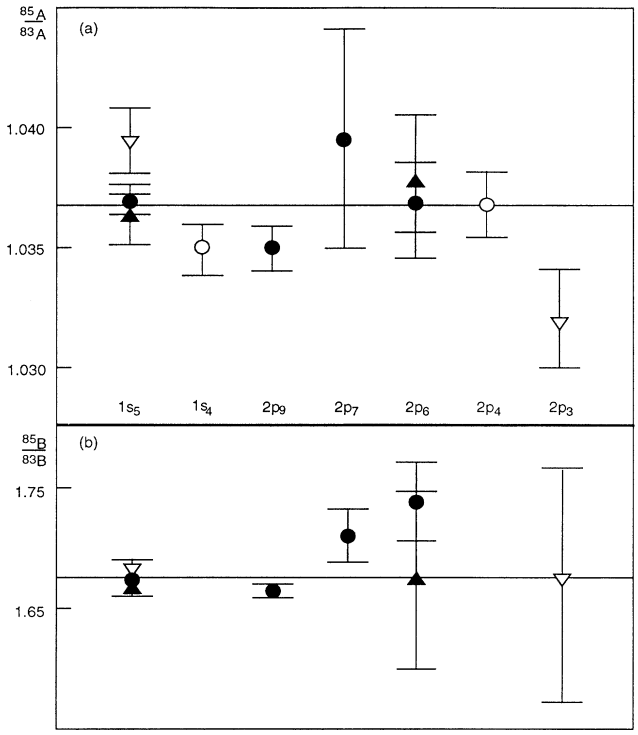

FIG. 6. Ratios of hyperfine constants of ^{85}Kr to ^{83}Kr; (a) $^{85}A/^{83}A$, (b) $^{85}B/^{83}B$. The solid circles are from this work, the solid triangles are from the work of Neugart [46], the empty circles are from [22] and the empty inverted triangles are from [23], which reported a hyperfine anomaly. The horizontal lines are the weighted average of all the data.

IV. DISCUSSION

In the first-order treatment, the isotope shift $\delta\nu_i^{A,A'}$ between isotopes with atomic masses A and A' can be expressed [2] as

$$\delta\nu_i^{A,A'} = F_i \delta\langle r^2\rangle^{A,A'} + \frac{A'-A}{AA'} M_i \tag{3}$$

for transition i. The first term is the field shift and the second term is the total mass shift. The field shift is the product of the change in the mean square nuclear charge radius $\delta\langle r^2\rangle^{A,A'}$ and the electronic factor for the transition F_i. The factor in the mass shift M_i depends on the transition but not the isotopes. A useful scaling relationship can be derived from Eq. (3) relating the isotope shifts of transition i to those of transition j:

$$\frac{AA'}{A'-A}\delta\nu_i^{A,A'} = \frac{AA'}{A'-A}\delta\nu_j^{A,A'}\frac{F_i}{F_j} + b_{ij}. \tag{4}$$

This linear relationship between scaled isotope shifts of different transitions is a consequence of the proportionality of all the field shifts of an element to a set of common nuclear properties: the changes in the mean square nuclear charge radius. The slope is the ratio of the electron-

ic factors F_i/F_j for the two transitions. The slope and the intercept b_{ij} in Eq. (4) depend on the electronic transitions but are independent of the isotopes.

A plot of the weighted isotope shifts used in Eq. (4) is called a King plot. The linearity of a King plot is a consistency check on the isotope shift data. King plots can also be used to predict the isotope shift of a rare isotope in a transition for which it has not been measured from the value in a transition where the isotope shift is known. This is a consequence of the isotopic independence of the slope and intercept in a King plot.

From the data in Table II for the odd-mass isotopes and in Table III in [14] for the even-mass isotopes, King plots were made. Figure 7 shows the King plot for the two transitions that have the most complete data sets: $1s_5$-$2p_6$ and $1s_5$-$2p_9$. Each point in Fig. 7 is labeled by the atomic mass numbers of the pair of isotopes. The slope of this King plot is 1.0(3), in agreement with the result of 1.0(3) from [14] on the even isotopes. A King plot with a slope of one means that the change in the electron density at the nucleus is the same for both transitions. This is to be expected for a pair of transitions from the same lower state to upper states of the same configuration.

The minimum and maximum values in Fig. 7 for both transitions belong to the pairs ^{85}Kr-^{83}Kr and ^{83}Kr-^{81}Kr, respectively. These isotope pairs correspond to the minimum and maximum change in $\delta\langle r^2\rangle^{A,A+2}$. It is also clear that the $\delta\langle r^2\rangle^{A,A+2}$ values vary irregularly among the isotopes. The variation in the mass weighting factor is not large enough to affect these conclusions. However, without knowing the mass shifts, even the signs of these $\delta\langle r^2\rangle$ values cannot be determined. The shifts for the odd-isotope pairs of the other transitions are consistent with the two transitions used in Fig. 7 and with the results of the even-mass isotopes [14].

For krypton, the relationships among the isotope shifts for different transitions can be expressed in a more useful form for the odd-mass isotopes because even-mass isotopes surround the odd-mass isotopes. The mass shift depends on $(A'-A)/AA'$. For $A'=A+2$, the approximation $2/[A(A+2)]=1/(A-1)(A+1)+1/(A+1)(A+3)$ is accurate to better than 0.5% for krypton isotopes. Thus, the mass-shift contribution to $\delta\nu^{83,85}$ is well approximated by the average mass shift of $\delta\nu^{82,84}$ and $\delta\nu^{84,85}$ or, equivalently, one-half the mass shift of $\delta\nu^{82,86}$. Subtracting one-half the isotope shift between the surrounding two even-mass isotopes from the bracketed odd-mass isotope shift leaves a term Δ_i that is the product of F_i and a factor that depends only on the $\delta\langle r^2\rangle$'s. These Δ_i's vary between two transitions as the slope of the King plot for these transitions. The advantage of this approach for krypton is that Δ_i is small, so the errors in the slopes of the King plots have a minimum effect on calculated isotope shifts. Table II lists these Δ_i's for the odd-mass isotope shifts. These deviations are on the order of 10 to 20 MHz. Within their combined errors, the ratios of the Δ's agree with the King plot slopes from [14].

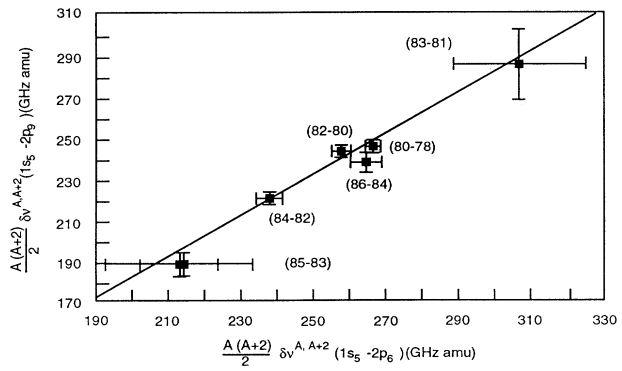

FIG. 7. King plot of the $1s_5$-$2p_6$ transition vs the $1s_5$-$2p_9$ transition in krypton. The numbers in parentheses identify the isotope pairs by atomic number. The data for (85-83) and (83-81) are from Table II and the even-mass isotope shift data are from [14]. The two points in the figure labeled (85-83) correspond to the two shifts listed in Table II for the ^{85}Kr-^{83}Kr isotope shift for the $1s_5$-$2p_6$ transition.

The first-order scaling relations for the hyperfine constants are reported in [23] to be in error for krypton by 0.8(3)% for the magnetic hyperfine constant. This reported hyperfine anomaly in krypton is based on the two extreme ratios in Fig. 6(a). The ratio for the $1s_5$ state from [23] is clearly above the other measured ratios for this state. The ratio $^{85}A/^{83}A$ for the $2p_3$ state has only been measured in [23], however, ^{83}A has been measured [14,16,18,19] by several groups. The disagreement from the average stems from the data for ^{85}Kr, not ^{83}Kr, of both the extreme $^{85}A/^{83}A$ ratios in Fig. 6(a). Some common systematic error might have affected both A values for that ^{85}Kr spectrum. The ^{85}Kr sample contained three times more ^{83}Kr than ^{85}Kr [24] and only two of the ^{85}Kr hyperfine lines are well resolved from ^{83}Kr lines in the sample spectrum shown in [24]. This might be the source of a small systematic error in these two ^{85}Kr hyperfine constants.

With the number of states represented in Fig. 6, we can look for correlations between the deviations from the average and those electronic configurations that should enhance nuclear volume effects for the hyperfine constants. Both the $1s_5$ and $1s_4$ states of krypton have the configuration $4p^5 5s$ with the $P_{3/2}$ ion core. These two states with their $5s$ outer electron should be more affected by the nuclear size corrections. However, there is no evidence of an effect in Fig. 6. Both the $2p_3$ and $2p_4$ states have the configuration $4p^5 5p$ with the $P_{1/2}$ ion core. The $P_{1/2}$ ion core can be described in terms of a configuration containing a $p_{1/2}$ hole. This $p_{1/2}$ hole should be more sensitive to the nucleus than the $p_{3/2}$ hole in the configuration of the $P_{3/2}$ ion core. Figure 6(a) includes data for the $2p_3$ and $2p_4$ states, and although the data point for the $2p_3$ state is about twice the error estimate below the average, the $2p_4$ state is right on the average. The $2p_9$, $2p_7$, and $2p_6$ states are all of the configuration $4p^5 5p$ with the $P_{3/2}$ ion core. These states should have minimal nuclear volume effects, but there is no systematic deviation between these states and those that should have

maximum nuclear volume effects. In conclusion, there is no obvious correlation between the configurations of the states and their deviations from Eqs. (2). In particular, no correlations exist such as would be expected for nuclear volume effects, hence there is no evidence of a hyperfine anomaly.

The other source of deviation from first-order scaling for hyperfine constants is J mixing. Mixing of different J states by the hyperfine Hamiltonian is most detectable in the ratios of the magnetic hyperfine constants. This sensitivity is because the magnetic-dipole hyperfine constants are measured with between one and two orders of magnitude higher precision than the quadrupole hyperfine constants. The correction to the magnetic-dipole hyperfine constant $\delta A(J)$ of a state with electronic angular momentum J due to mixing by the hyperfine Hamiltonian with state J' is given by [6]

$$\delta A(J) \propto \sum_{k_1,k_2} (-1)^{k_1+k_2} \langle I \| T(n)^{k_1} \| I \rangle \langle I \| (T)(n)^{k_2} \| I \rangle \times \frac{\langle J \| T(e)^{k_1} \| J' \rangle \langle J' \| T(e)^{k_2} \| J \rangle}{E_J - E_{J'}}, \quad (5)$$

where $k_1, k_2 = 1$ or 2, and $E_J - E_{J'}$ is the energy separation between the two states. The missing proportionality constant depends on 3-j and 6-j symbols involving I, J, J', k_1, and k_2. The reduced matrix elements of the nuclear operators $T(n)^1$ and $T(n)^2$ are proportional to the magnetic-dipole and electric-quadrupole moments, respectively. The diagonal matrix elements of the electronic operators $T(e)^1$ and $T(e)^2$ give, respectively, the magnetic field and electric field gradient at the nucleus due to the electrons. These diagonal matrix elements are proportional to the respective hyperfine constants to first order.

This correction will be a maximum for a state with a small $E_J - E_{J'}$ and large electronic matrix elements. The correction $\delta A(J)$ will have a large isotopic dependence for the terms involving the quadrupole moment because of the large differences in the quadrupole moment between isotopes. The smallest energy separation of the states studied is for the $2p_9$ state. The $2p_9$ state is only 13 cm^{-1} from the $2p_8$ state, which has the same configuration as and can be mixed with the $2p_9$ state. The large dipole and quadrupole hyperfine constants for both these states [14] suggest that these off-diagonal electronic reduced matrix elements will also be large. These factors, combined with the good precision on the $^{85}A/^{83}A$ ratio, make the $2p_9$ state a prime candidate for detecting the effects of J mixing by the hyperfine interaction.

To estimate an upper limit for this correction, I substituted the maximum diagonal reduced matrix elements for this electronic configuration for the off-diagonal elements. This is a reasonable upper limit because the electronic matrix elements depend predominantly on the $4p$ electrons [19], which are the same for both these states. The diagonal reduced matrix elements were calculated from the measured hyperfine constants using equations given in [6]. This correction changes about 100% in going from ^{83}Kr to ^{85}Kr because of the large change in the electric-quadrupole moment. From this estimate, J mixing corrections to A for the $2p_9$ state are less than 0.01%, more than an order of magnitude smaller than my error estimates for A of this state.

In this worst case, J mixing is less than a 0.01% correction to the first-order scaling. The full sets of data in Figs. 5 and 6 do not support a hyperfine anomaly in krypton. Thus the scaling of the hyperfine constants in Eqs. (2) is accurate to at least the experimental uncertainty: 0.1% for ratios of A's and 1% for ratios of B's. With this accuracy, scaling of ^{83}Kr hyperfine constants to calculate ^{81}Kr and ^{85}Kr hyperfine constants can predict hyperfine splittings to within a few megahertz. The only exception to these accurate predictions should occur when the separation between J mixed states is 1 cm^{-1} or less.

The electronic state independence of the hyperfine constant ratios shown in Figs. 5 and 6 does not directly test Eqs. (2). The ratios on the right-hand sides of Eqs. (2) have not been directly measured nor their equality with the left-hand sides demonstrated. However, the range of electronic configurations represented in Figs. 5 and 6 includes the outer electron in $5s$, $5p$, and $5d$ orbitals and both ion core configurations. Only the closed inner shells are unchanged. Given this range of configurations, I think it unlikely that the error in Eqs. (2) is significant in the determination of the nuclear moments of ^{81}Kr and ^{85}Kr. Tables VII and VIII compare the nuclear moments of the three odd-mass krypton isotopes with those of the strontium and selenium isotopes [45] having the same number of neutrons. The moments of ^{81}Kr determined in this work fit well with the trends of elements having two more or two fewer protons.

The striking difference in the line shapes between the even- and odd-mass isotopes of the saturation spectrum shown in Fig. 3 can be explained by collisional energy transfer. Each peak in the saturation spectrum is composed of a broad Gaussian and a narrow Lorentzian component. In Fig. 3, the amplitude ratio of the broad component to the narrow component is 10:1 for ^{86}Kr and 1:3 for the ^{85}Kr line at +1400 MHz. These amplitude ratios change with pressure, laser intensity, and beam diameters. But the broad component is always a much larger fraction of the peak for ^{86}Kr than for ^{85}Kr. This is a general difference between the even and odd krypton isotopes.

TABLE VII. Comparison of the nuclear magnetic-dipole moments (in nuclear magnetons) of ^{81}Kr, ^{83}Kr, and ^{85}Kr with strontium and selenium isotopes having the same number of neutrons N. The proton number for each element is given as a subscript to the left of the chemical symbol. The values for ^{81}Kr and ^{85}Kr are from this work; the other values are from [45].

Isotope \ N	45	47	49
$_{34}$Se	−1.018(15)		
$_{36}$Kr	−0.909(4)	−0.970 669(3)	−1.005 5(4)
$_{38}$Sr	−0.829 8(3)	−1.000 5(3)	−1.093 603 0(13)

TABLE VIII. Comparison of the electric-quadrupole moments (in barns) of ^{81}Kr, ^{83}Kr, and ^{85}Kr with strontium and selenium isotopes having the same number of neutrons N. The proton number for each element is given as a subscript to the left of the chemical symbol. The values for ^{81}Kr and ^{85}Kr are from this work; the other values are from [45].

Isotope \ N	45	47	49
$_{34}$Se	+0.8		
$_{36}$Kr	+0.629(13)	+0.253(5)	+0.433(8)
$_{38}$Sr	+0.823(50)	+0.323(20)	+0.335(20)

The broad Gaussian component is produced by two collision processes for transitions from Kr($1s_5$) [35]: velocity-changing collisions and metastability-exchanging collisions. Velocity-changing collisions change the velocity of a Kr($1s_5$), but the excitation stays with the initially excited atom. Metastability-exchanging collisions transfer the $1s_5$-state excitation between the collision partners. The cross section for metastability exchange is almost twice that for velocity change [35]. These two collision processes can also explain the line-shape difference between the even- and odd-mass isotopes.

The line shapes of the even isotopes are dominated by ^{even}Kr+^{even}Kr($1s_5$) collisions because even-mass isotopes are in large excess. Similarly ^{even}Kr+^{odd}Kr($1s_5$) collisions dominate the line shapes of the odd isotopes. Even-even collisions generate a Doppler background and diffusion out of the laser beam is the main loss mechanism for the even-isotope Doppler background [35]. The odd-isotope Doppler background is smaller for two reasons. First, even-odd collisions have a lower rate of generating an odd-isotope Doppler background because metastability exchange generates a Doppler background for the even isotopes. Second and more important, metastability exchange in even-odd collisions provides an additional loss mechanism for the odd-isotope Doppler background. The odd-isotope Doppler background relaxes into the even-isotope population by metastability exchange. Relaxation of the even-isotope Doppler background into the odd-isotope population is negligible in these samples containing mostly even isotopes. Thus both the rate of production is smaller and the loss rate is larger for the odd-isotope Doppler background than for the even-isotope Doppler background. This mechanism depends on the larger abundance of the even isotopes and not on the isotopes being even or odd.

The ratios of the amplitudes of the narrow to broad components in this work are consistent with the cross sections and formulas given in [35]. The relatively large beam diameters used in this work accentuate this difference in peak shapes because they result in longer times to diffuse out of the laser beam. Because the discharge implants krypton in the cell walls, the pressure is not known accurately enough for the present results to give a stringent test of this model or the cross sections [35]. The odd-isotope line shapes may also be influenced by collisions that transfer atoms between hyperfine levels. Experiments to test whether this mechanism is significant in the present work would again need accurate measurements of the krypton pressure.

ACKNOWLEDGMENTS

I would like to thank Frank Shima at the National Institutes of Standards and Technology for the donation of the ^{81}Kr sample. I would also like to thank Rainer Neugart and co-workers at the Institüt für Physik, Universität Mainz for sharing their ^{81}Kr and ^{85}Kr hyperfine data. This work was sponsored at Pacific Northwest Laboratory by the Director, Office of Basic Energy Sciences, Chemical Sciences Division of the U.S. Department of Energy under Contract No. DE-AC06-76RLO 1830. Pacific Northwest Laboratory is operated for the U.S. Department of Energy by Battelle Memorial Institute.

[1] Lloyd Armstrong, Jr., *Theory of the Hyperfine Structure of Free Atoms* (Wiley-Interscience, New York, 1971), Chap. 1.
[2] K. Heilig and A. Steudel, At. Data Nucl. Data Tables **14**, 613 (1974).
[3] P. Aufmuth, K. Heilig, and A. Steudel, At. Data Nucl. Data Tables **37**, 455 (1987).
[4] R. Beigang, E. Matthias, and A. Timmermann, Phys. Rev. Lett. **47**, 326 (1981).
[5] Jun-Qiang Sun, K. T. Lu, and R. Beigang, J. Phys. B **22**, 2887 (1989).
[6] G. K. Woodgate, Proc. R. Soc. London, Ser. A **293**, 117 (1966).
[7] R.-J. Champeau and J.-C. Keller, J. Phys. B **11**, 391 (1978).
[8] C. Brechignac and S. Gerstenkorn, J. Phys. B **10**, 413 (1977).
[9] D. A. Jackson, J. Opt. Soc. Am. **69**, 503 (1979).
[10] H. Gerhardt, E. Matthias, H. Rinneberg, F. Schneider, A. Timmermann, R. Wenz, and P. J. West, Z. Phys. A **292**, 7 (1979).
[11] D. A. Jackson, J. Opt. Soc. Am. **70**, 1139 (1980).
[12] C. Brechignac, J. Phys. B **10**, 2105 (1979).
[13] T. Trickl, M. J. J. Vrakking, E. Cromwell, T. Y. Lee, and A. H. Kung, Phys. Rev. A **39**, 2948 (1989).
[14] B. D. Cannon and G. R. Janik, Phys. Rev. A **42**, 397 (1990).
[15] J. R. Brandenberger, Phys. Rev. A **39**, 64 (1989).
[16] S. C. Parker and J. R. Brandenberger, Phys. Rev. A **44**, 3354 (1991).
[17] W. L. Faust and L. Y. Chow Chiu, Phys. Rev. **129**, 1214 (1963).
[18] D. A. Jackson, J. Opt. Soc. Am. **67**, 1638 (1977).
[19] X. Husson, J.-P. Grandin, and H. Kucal, J. Phys. B **12**, 3883 (1979).
[20] H. Abu Safia and X. Husson, J. Phys. (Paris) **45**, 863 (1984).
[21] H. A. Schuessler, A. Alousi, R. M. Evans, M. Brieger, F.

Buchinger, and Y. F. Li, Phys. Rev. Lett. **65**, 1332 (1990).
[22] E. Rasmussen and V. Z. Middelboe, Z. Phys. **141**, 160 (1955).
[23] H. Gerhardt, F. Jeschonnek, W. Makat, E. Matthias, H. Rinnenberg, F. Schneider, A. Timmermann, R. Wenz, and P. J. West, Hyperfine Interact. **9**, 175 (1981).
[24] G. Gerhardt and E. Matthias, Kvant. Elektron. (Moscow) **4**, 2624 (1977) [Sov. J. Quantum Electron. **7**, 1500 (1977)].
[25] G. S. Hurst, C. H. Chen, S. D. Kramer, Raymond Davis, Jr., Bruce Cleveland, Fletcher Gabbard, and F. J. Schima, Phys. Rev. Lett. **53**, 1116 (1984).
[26] B. E. Lehmann and H. H. Loosli, in *Resonance Ionization Spectroscopy 1984,* Proceedings of the Second International Symposium on Resonance Ionization Spectroscopy and its Applications, edited by G. S. Hurst and M. G. Payne, IOP Conf. Proc. No. 71 (Institute of Physics and Physical Society, Bristol, 1984).
[27] R. D. Willis, N. Thonnard, M. C. Wright, B. E. Lehmann, and D. Rauber, in *Resonance Ionization Spectroscopy 1988,* Proceedings of the Fourth International Symposium on Resonance Ionization Spectroscopy and its Applications, edited by T. B. Lucatorto and J. E. Parks, IOP Conf. Proc. No. 94 (Institute of Physics and Physical Society, Bristol, 1988).
[28] B. E. Lehmann, H. H. Loosli, D. Rauber, N. Thonnard, and R. D. Willis, Appl. Geochem. **6**, 419 (1991).
[29] J. N. Andrews, T. Florkowski, B. E. Lehmann, and H. H. Loosli, Appl. Geochem. **6**, 425 (1991).
[30] B. D. Cannon and T. J. Whitaker, Appl. Phys. B **38**, 57 (1985).
[31] J. J. Snyder, T. B. Lucatorto, P. H. Debenham, and S. Geltman, J. Opt. Soc. Am. B **2**, 1497 (1985).
[32] W. M. Fairbank, Jr., Nucl. Instrum. Methods B **29**, 407 (1987).
[33] N. Thonnard, R. D. Willis, M. C. Wright, W. A. Davis, and B. E. Lehmann, Nucl. Instrum. Methods B **29**, 398 (1987).
[34] B. D. Cannon (unpublished).
[35] C. Brechignac and R. Vetter, Phys. Rev. A **22**, 496 (1980).
[36] C. E. Moore, *Atomic Energy Levels,* Natl. Bur. Stand. (U.S.) Circ. No. 467 (U.S. GPO, Washington, DC, 1952), Vol. 2.
[37] Fred C. Gabriel, Rev. Sci. Instrum. **47**, 484 (1976).
[38] W. W. Macalpine and R. O. Schildknecht, Electronics **33**, 140 (1960).
[39] H. S. Butler and G. S. Kino, Phys. Fluids **6**, 1346 (1963).
[40] A. O. R. Cavaleru, D. G. Armour, and G. Carter, Vacuum **22**, 321 (1972).
[41] B. Dahmani, L. Hollenberg, and R. Drullinger, Opt. Lett. **12**, 876 (1987).
[42] B. A. Bushaw, B. D. Cannon, G. K. Gerke, and T. J. Whitaker, Opt. Lett. **11**, 422 (1986).
[43] Victor Kaufman and Curtis J. Humphreys, J. Opt. Soc. Am. **59**, 1614 (1969).
[44] Lloyd Armstrong, Jr., Ref. [1], Chap. 7.
[45] Pramila Raghavan, At. Data Nucl. Data Tables **42**, 189 (1989).
[46] R. Neugart (private communication).